Supporting information

Solvothermal Phase Change Induced Morphology Transformation in $CdS/CoFe_2O_4@Fe_2O_3$ Hierarchial Nanosphere Arrays as Ternary Heterojunction Photoanodes for Solar Water Splitting

Soumyajit Maitra[1], Arundhati Sarkar[2], Toulik Maitra[1], Somoprova Halder[1], Kajari Kargupta[2], Subhasis Roy[1*]

[a]Department of Chemical Engineering, University of Calcutta, 92, APC Road, Kolkata, West Bengal 700009, India. [b]Department of Chemical Engineering, Jadavpur University, 88, Raja Subodh Chandra Mallick Rd, Jadavpur, Kolkata, West Bengal 700032, India
*Corresponding author. Tel.: +91-9775032952 (mobile), +9133-2350-8386/6396 (ext. 256) (office), E-mail address: subhasis1093@gmail.com, srchemengg@caluniv.ac.in

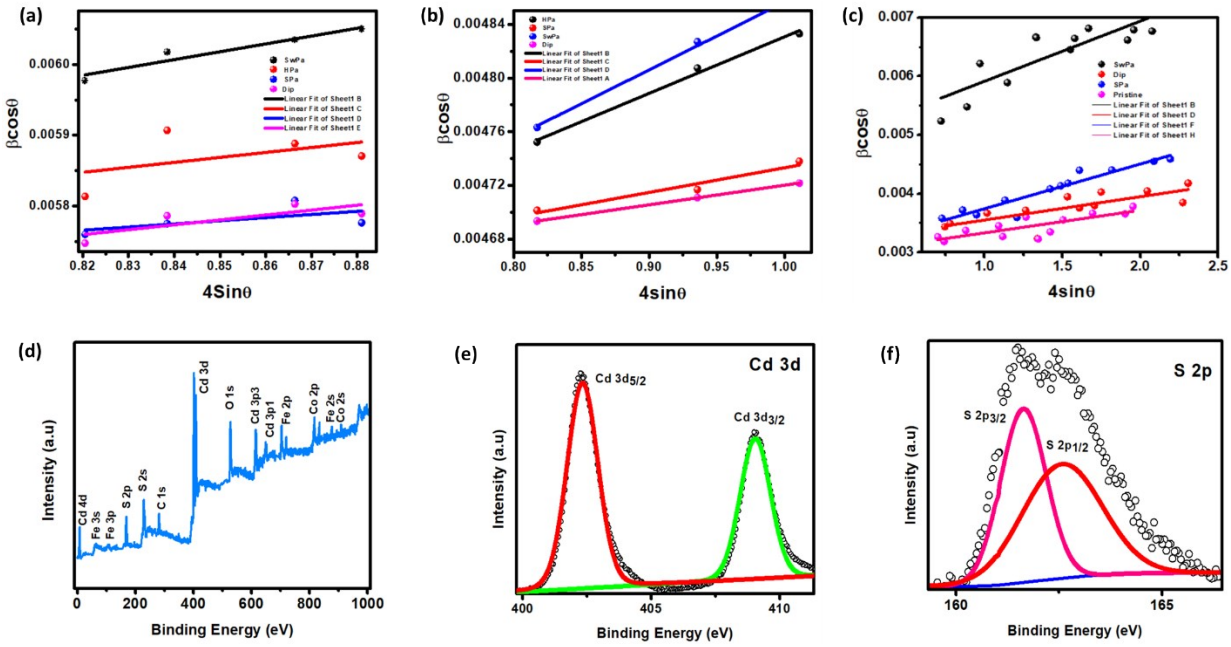

Figure S1 (a) Williamson Hall plots of CdS present in the fabricated photoanodes (b) Williamson Hall plots of $CoFe_2O_4$ present in the fabricated photoanodes (c) Williamson Hall plots of Fe_2O_3 present in the fabricated photoanodes (d) Full XPS scan (e) XPS spectra of Cd 3d core level (f) XPS spectra of S 2p core level

Hall-Williamson Plots were used here instead of the Scherrer equation for calculation of crystallite size as ordered growth of nanostructures and formation of vacancies result in an increased strain that contributes to the increase in FWHM apart from only the broadening caused by crystallite size change. The equations used for calculations were as follows[1]

$$\beta cos\theta = 4\epsilon sin\theta + \frac{k\lambda}{D} \quad \text{... (1)}$$

$$\delta = \frac{1}{D^2} \quad \text{... (2)}$$

Where β is the FWHM, ϑ is the ½ of the angle of diffraction, δ is the dislocation density, ϵ is the lattice strain, λ is the wavelength of Cu Kα X-rays and D is the crystallite size. From the plot between $cos\theta \; and \; 4sin\theta$, the slope provides the value of lattice strain and the intercept provides the value of crystallite size.

The homogenous component of lattice strain caused due to uniform lattice contraction was measured by calculating root mean squared strain $< \epsilon_{RMS} >$ from the following equation[1]

$$< \epsilon_{RMS} >= (^{2}/_{\pi})^{1/2} \frac{\Delta d_{hkl}}{d_{0hkl}} \quad \text{... (3)}$$

Where Δd_{hkl} indicated the difference in lattice spacing between ideal values in the JCPDS database and experimentally measured values. d_{0hkl} describes the ideal lattice spacing given in the JCPDS database.

The FWHM of (311) peak for the CoFe2O4 of sample Dip was larger than sample (SPa) primarily as the strain developed due to formation of a thin shell of cobalt ferrite by rapid diffusion of surface adsorbed ions at high temperature was supposedly higher than the solvothermal pathway where slow thermodynamic control ensures formation of a more stable phase. The crystallite size for the sample Dip was 26.15 nm and the strain calculated from the slope of the plot was 6.937E-4. The crystallite size obtained for sample SPa was slightly smaller and was 25.66 nm while the slope corresponding to strain was much lower at approximately 4.451E-4 . Cobalt ferrite present in sample SwPa showed the highest strain of 0.0011 and smallest crystallite size of 18.11nm as expected. In the sample HPa, strain in cobalt ferrite was reduced a little bit to 7.022E-4 and crystallite size was slightly increased to 20.91 nm. The dislocation density for the samples Dip, SPa, SwPa, HPa were measured to be approximately 1.462E-3, 1.52E-3, 3.18E-3 and 2.26E-3. The higher dislocation density for SPa compared to Dip can be attributed to the fact that etching and exfoliation of nanoplates caused by surfactants followed by Co^{2+} impregnation may have resulted in higher crystal defects. The obtained root mean squared strain for the Cobalt ferrite (110) peaks were approximately 0.004 for all the samples.

Hall-Williamson plots revealed that the smooth CdS coated nanospheres in sample Dip had the lowest strain of 1.46E-4 and crystallite size of 30.32 nm. The toothlike nanostructures in the sample SPa resulted in an increase in strain to 1.83E-4 with a slightly increased crystallite size of 30.8 nm. The CdS nanoparticle aggregates formed on sample HPa and SwPa showed very high strains of 4.21E-4 and 5.04E-4 respectively and much smaller crystallite sizes of 24.2 nm and 23.89 nm respectively. Thus, we can conclude that roughness and porosity of substrate on which nucleation is taking place plays a key role in controlling the morphology and structural properties of deposited CdS

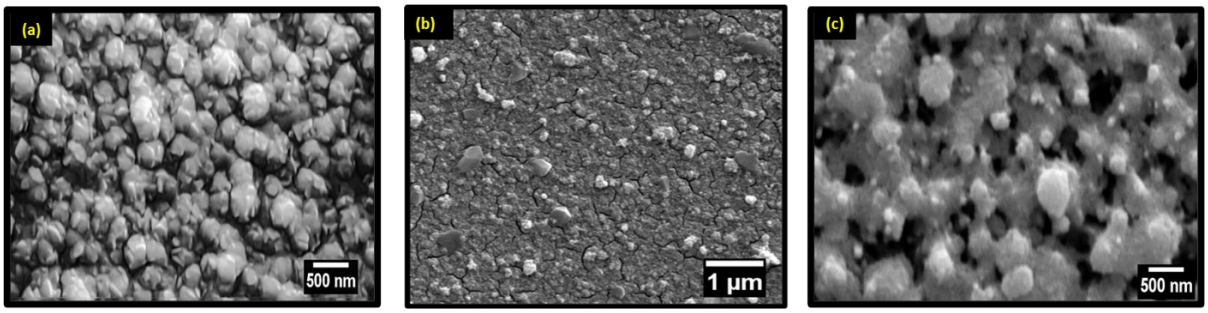

Figure S2 (a) Dip without CdS (b) HPa without CdS at low magnification (c) HPa at low magnification

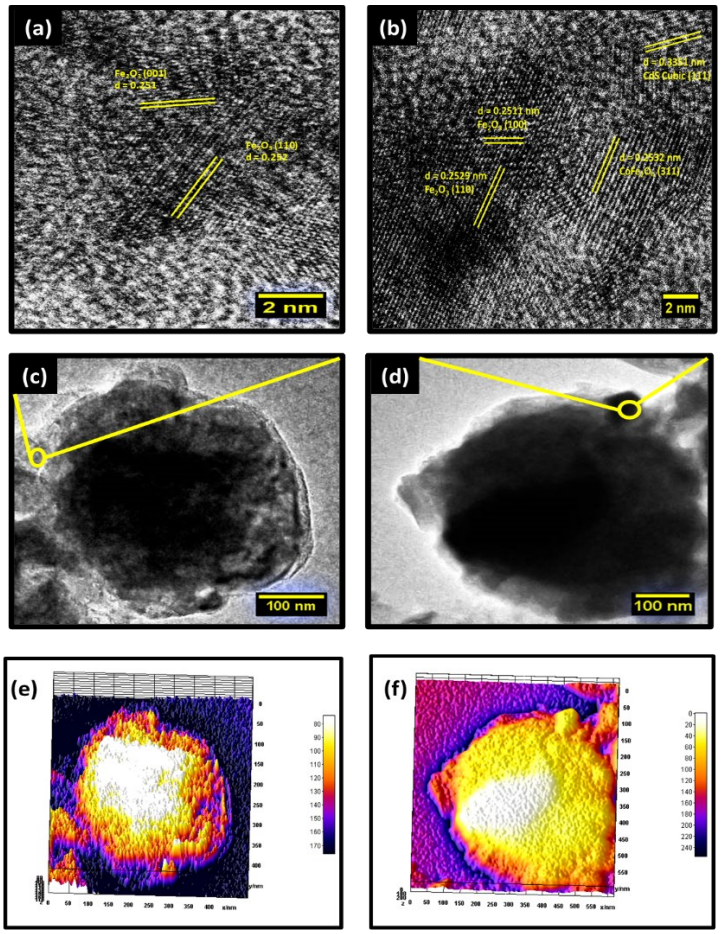

Figure S3 (a) TEM images lattice fringes of Pristine hematite (b) TEM images lattice fringes of sample SPa (b) TEM image of pristine hierarchial nanosphere hematite (d) TEM image of hierarchial nanosphere of ternary heterojunction sample SPa (e) 3D TEM image reconstruction of pristine hierarchial nanosphere hematite (f) 3D TEM image reconstruction of pristine hierarchial nanosphere of ternary heterojunction sample SPa

The TEM images of pristine hematite hierarchial nanospheres present in fig S3 (a) and (c) indicate the presence of (110) facets crystal facet tailored nanostructure. Fig S2 (b) and (d) indicate the presence of $CoFe_2O_4$ and CdS in the ternary heterojunction hierarchial nanosphere due to the presence of characteristic (311) facet for cobalt ferrite and (111) facet for cubic CdS. The area for TEM imaging has been labelled in yellow as an area that was selectively chosen where all the three materials in the ternary heterojunction were distinctly visible due to varying material thickness in the nanostructures. Figure S2 (e)and (f) indicate the 3D reconstruction of Fig S2 (c) and (d). The varying depths mapped using colour mapping and image analysis indicate the contours of the core-shell nature of the ternary heterojunction nanospheres.

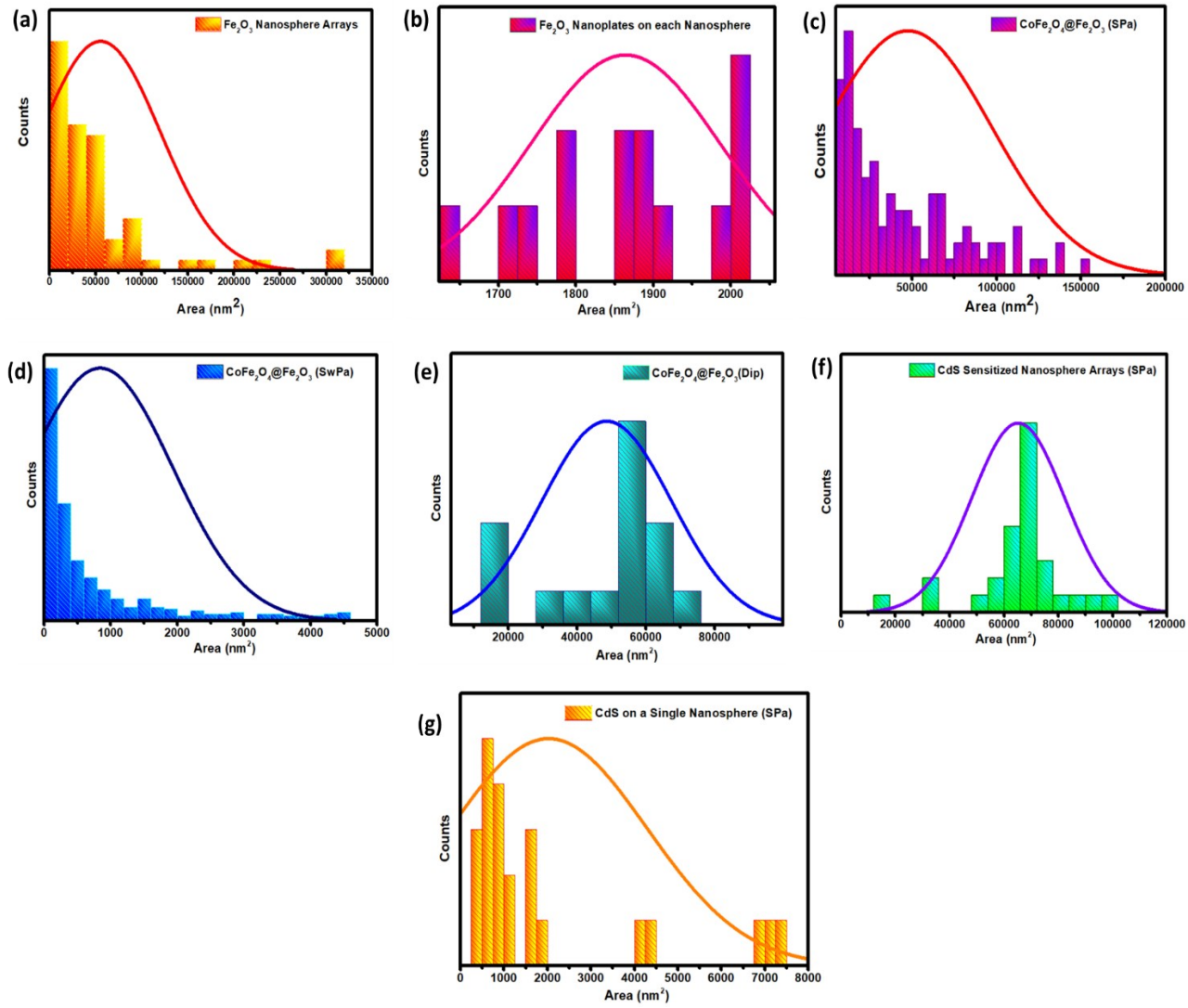

Figure S4 (a) Historam plots indicating the area distribution of (b) pristine hematite nanosphere arrays (c) hematite nanoplates on each hierarchial nanosphere (d) CoFe2O4@Fe2O3 nanospheres for sample SPa (e) CoFe2O4@Fe2O3 nanospheres for sample Dip (f) CdS sensitized nanosphere arrays for sample SPa (g) CdS protrusions on each nansphere for sample SPa

Histogram plots in fig S4 were used to indicate the area distribution of the nanostructures under the influence of different synthesis conditions. Histogram plots were constructed using image analysis. The hematite hierarchial nanospheres showed a mean area of 51233.71 $nm^{2,}$ with the mean area of the nanoplate-like protrusions on each nanosphere to be approximately 1863.92 nm^2. The CoFe2O3@Fe2O3 showed a mean area of 57731.66 nm^2 for sample SPa while that for sample Dip was 59156.83. The increase in area for Dip was due to the fact that image analysis does not take into consideration the porosity of the nanostructures, but only the diameter of the spherical nanostructures which was found to decrease in SPa due to the etching assisted porosity enhancement. CdS sensitization caused an increase in the area resulting in an increase in mean area to 67693.36 nm^2. CdS toothlike protrusions were found to have an area distribution of 1978.67 nm^2. These factors indicate the importance of hierarchial nanostructuring as individual secondary protrusions significantly increase the nanostructures in addition to the overall area of the primary structure.

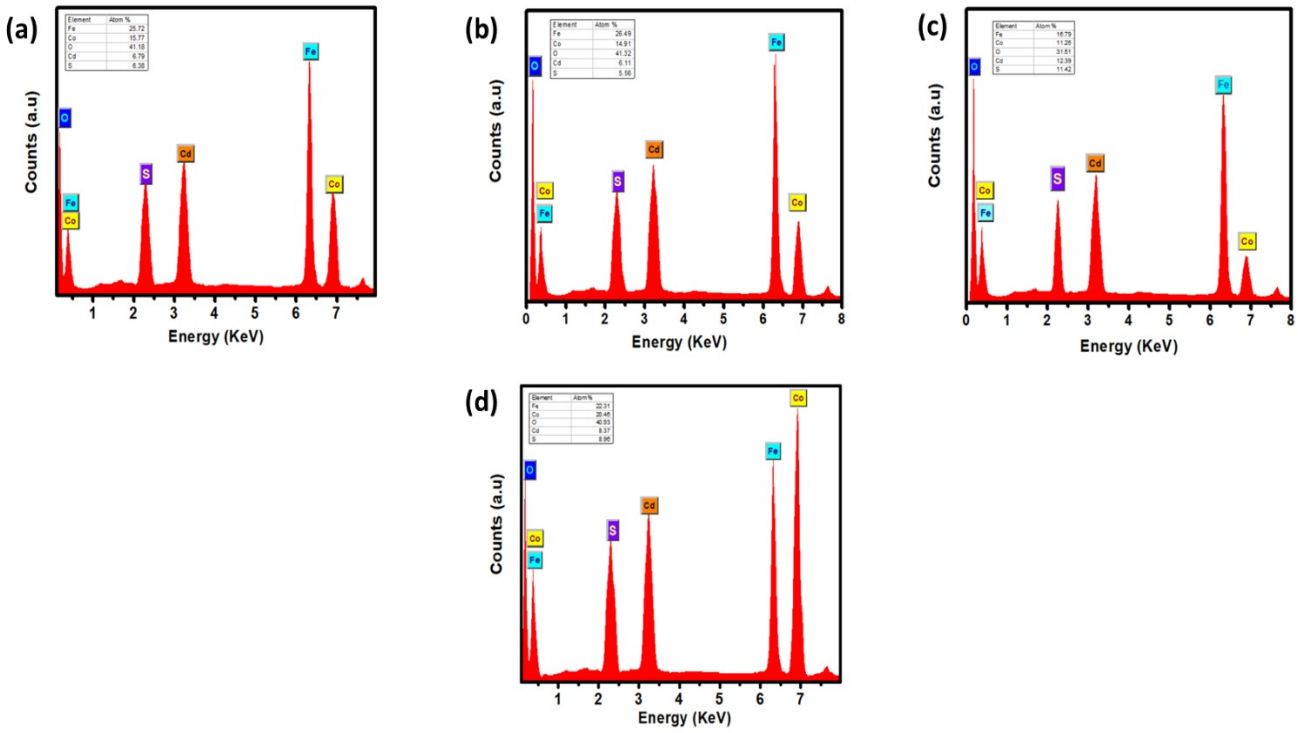

Figure S5. EDAX plots for samples (a) SPa (b) Dip (c) SwPa (d) HPa

EDAX mapping was carried out to analyse the atomic constitution of the fabricated photoanodes. The atom % for Co was highest in sample HPa due to the presence of unreacted CoO on top of the impurity phase. SwPa showed the lowest amounts of Fe and Co due to stripping away of the film caused by the lack of pre-annealing. The amount of Co in sample SPa was found to be slightly higher than Dip due to phase change assisted porosity enhancement in the solvothermal process.

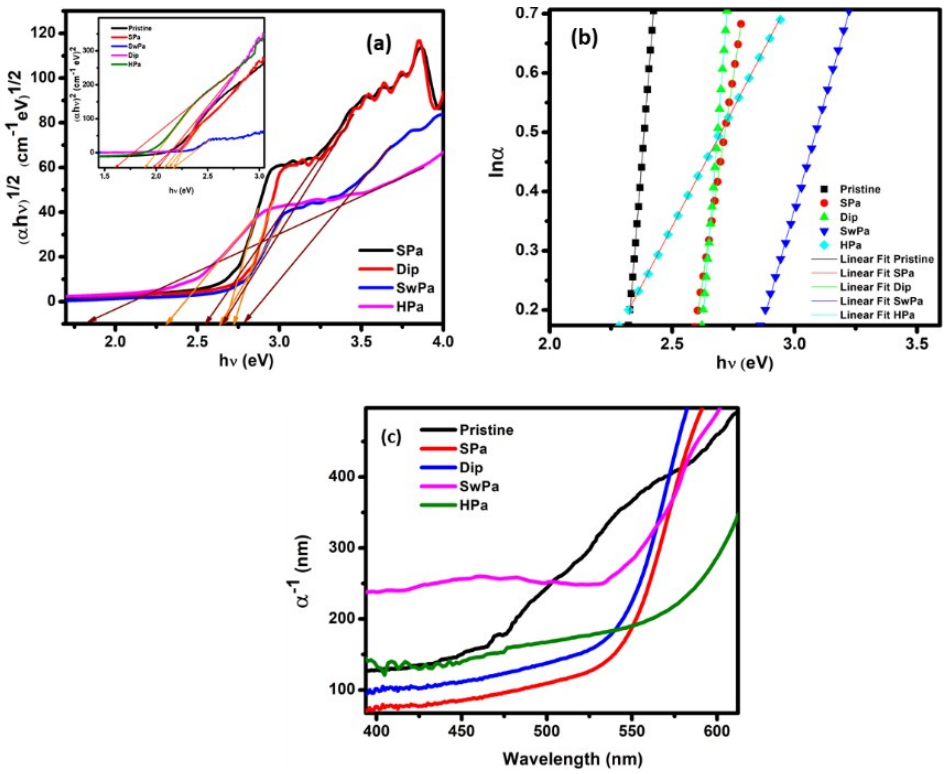

Figure S6. (a) Tauc plots for direct bandgap of the fabricated photoanodes with indirect bandgap in the inset (b) Urbach energy plots for the fabricated photoanodes (c) Penetration depth plots for the fabricated photoanodes

Urbach energy and penetration depth is shown in Fig S7 (b) and (c) was calculated from the following equations[2,3]

Penetration depth = $\frac{1}{\alpha}$, where $\alpha = \frac{2.303\ A}{t}$ ...(4)

$$\ln \alpha = lna_0 + \frac{h\vartheta}{E_u} \quad ...(5)$$

Where α is the coefficient of absorption, A is absorbance, t is film thickness measured in nm, $h\vartheta$ is photon energy, and E_u is Urbach energy. Urbach energy is defined as the band tail width of inter-band localized states and is a measure of dislocation density and crystal defects present in the structure Penetration depth is defined as the thickness of films required for light to pass through for 63% absorption. Small penetration depth is an important criterion for photoelectrodes to ensure that majority of the light gets absorbed within the space charge region.

The lowest penetration depth of 71.8 nm was observed for that of SPa at 470 m, while the pristine hematite showed a depth of 127 nm at the same wavelength. This highlights the development of a ternary heterojunction photoanode where the presence of $CoFe_2O_4$ and CdS significantly increased light absorption and lowered penetration depth by a drastic margin, compared to the pristine substrate indicating enhanced light utilization resulting in increased generation of photoexcited charge carriers. In the region between 450 nm to 500 nm in figure 3(c), the penetration depth for pristine hematite significantly increased to 175.6 nm, while that for the sample SPa remained at a lower value of 94.6 nm. The sample SwPa showed the highest penetration depth, probably attributed to the low absorbance caused by severe morphological damage due to stripping away of hematite as a result of lack of pre-annealing. The penetration depth of HPa was lower than pristine hematite from 450 nm onwards due to the presence of large amounts of impurity phases like CoO and excessive amounts of defect states as evident from the PL spectra in

figure 5 which, despite increasing overall absorbance and lowering penetration depth, have a grave impact on photoelectrochemical performance.

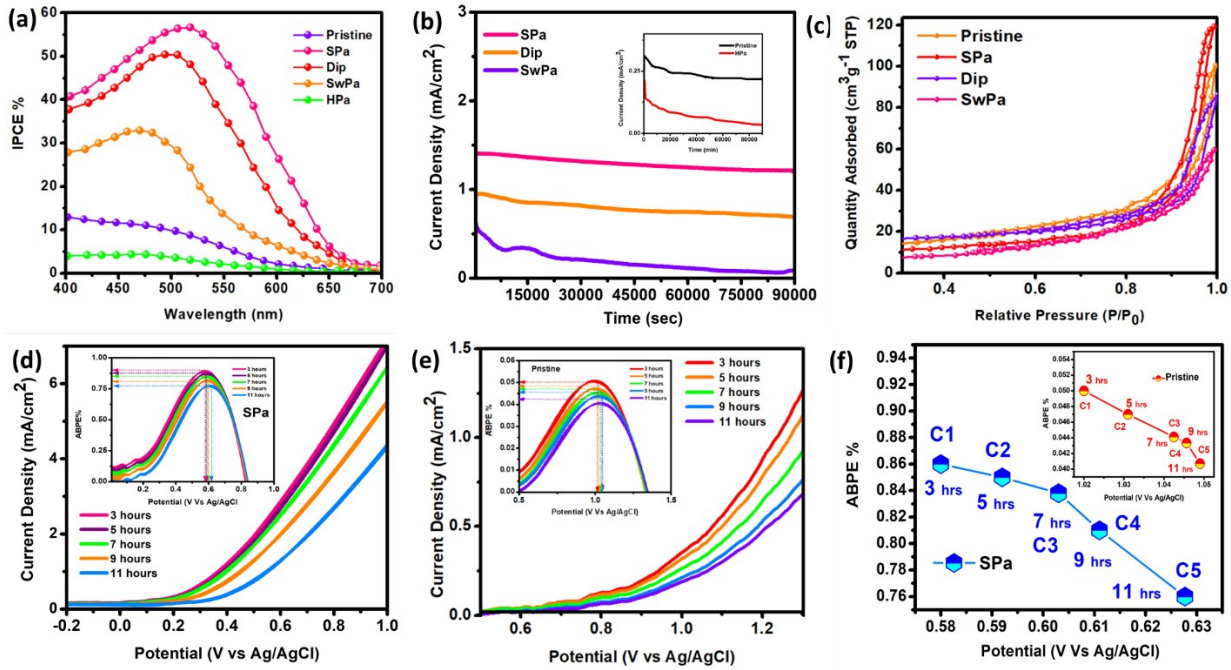

Figure S7. (a) IPCE % plots of the fabricated photoanodes (b) Chronoamperomety plots of the fabricated photoanodes (c) BET analysis plots of the fabricated photoanodes. (d) LSV plots with sample cycling with ABPE% plots (inset) for SPa (e) LSV plots with sample cycling with ABPE% plots (inset) for Pristine (f) Change in ABPE % for sample SPa with Pristine (inset)

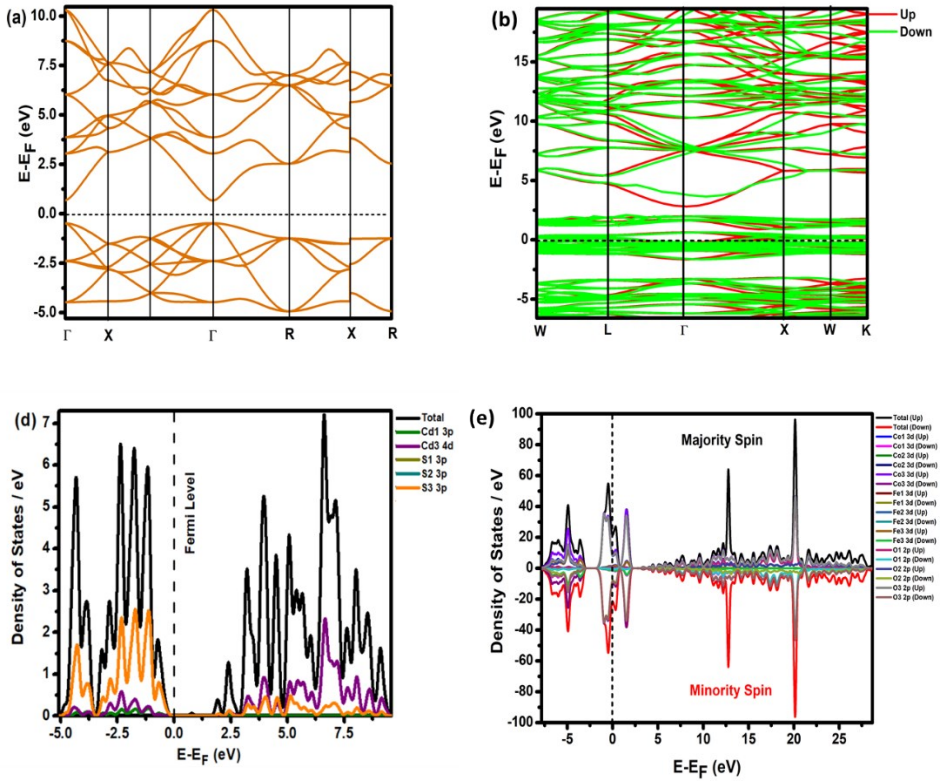

Figure S8. Band structure plots for (a) bulk CdS (b) bulk CoFe2O4 (c) DOS plots for bulk CdS (d) DOS plots for bulk CoFe2O4

Band structure and DOS plots for bulk CdS are shown in fig S8 (a) and (c). it can be observed that the CdS is a direct bandgap semiconductor with a bandgap of 2.2 eV as expected[4–6]. The DOS plots indicate the presence of hybridisation between the S 3p and Cd 3p orbitals as the primary contributor for the valence band, while the Cd 4d orbitals are the prime contributors to the conduction band. The VBM and CBM met at the Γ point, indicating the presence of a direct bandgap. Cobalt ferrite was observed to have an indirect bandgap with a slight offset at the Γ point for spin upstate, while a direct bandgap is observed for the spin downstate where the CBM and VBM meet at the Γ point (Fig S8b). The valence band in cobalt ferrite is primarily comprised of hybridization between the O 2p and Fe 3d and Co 3d orbitals while the CB is comprised of Fe 3d and Co 3d orbitals (Fig S8e). A significant overlap between the Fe 3d orbitals and Co 3d orbitals is observed in the V.B, which was absent in the C.B.

References

1 P. Bindu and S. Thomas, *Journal of Theoretical and Applied Physics*, 2014, **8**, 123–134.

2 V. R. Akshay, B. Arun, G. Mandal and M. Vasundhara, *Physical Chemistry Chemical Physics*, 2019, **21**, 12991–13004.

3 M. E. A. Warwick, K. Kaunisto, D. Barreca, G. Carraro, A. Gasparotto, C. Maccato, E. Bontempi, C. Sada, T. P. Ruoko, S. Turner and G. van Tendeloo, *ACS Applied Materials and Interfaces*, 2015, **7**, 8667–8676.

4 L. Cheng, Q. Xiang, Y. Liao and H. Zhang, *Energy and Environmental Science*, 2018, **11**, 1362–1391.

5 S. K. Gupta, K. Sudarshan, P. S. Ghosh, A. P. Srivastava, S. Bevara, P. K. Pujari and R. M. Kadam, *Journal of Materials Chemistry C*, 2016, **4**, 4988–5000.

6 J. Liu, *Journal of Physical Chemistry C*, 2015, **119**, 28417–28423.